PAPER • OPEN ACCESS

First SOLPS-ITER predictions of the impact of cross-field drifts on divertor and scrape-off layer conditions in double-null configuration of STEP

To cite this article: J. Karhunen *et al* 2024 *Nucl. Fusion* **64** 096021

OPEN ACCESS
IOP Publishing | International Atomic Energy Agency
Nuclear Fusion
Nucl. Fusion **64** (2024) 096021 (10pp)
https://doi.org/10.1088/1741-4326/ad63ba

First SOLPS-ITER predictions of the impact of cross-field drifts on divertor and scrape-off layer conditions in double-null configuration of STEP

J. Karhunen[1,*], S.S. Henderson[2], A. Järvinen[1], D. Moulton[2], S. Newton[2] and R.T. Osawa[2]

[1] VTT Technical Research Centre of Finland, PO Box 1000, 02044 VTT, Finland
[2] UKAEA, Culham Science Centre, Abingdon OX14 3DB, United Kingdom of Great Britain and Northern Ireland

E-mail: juuso.karhunen@vtt.fi

Received 15 January 2024, revised 20 June 2024
Accepted for publication 16 July 2024
Published 31 July 2024

Abstract

Introduction of cross-field drifts in SOLPS-ITER simulations of connected double-null plasmas in STEP with the ion $\nabla B \times B$ drift towards the upper divertors was found to enhance the detachment of the inner divertors with decreased target densities and ion and heat fluxes, while simultaneously complicating the access to detachment in the outer lower divertor by increasing the target temperature and heat loads to levels above the engineering limits. The $\nabla B \times B$ drift was observed to significantly affect the radial heat transport between the core and the scrape-off layer (SOL), altering the poloidal temperature and pressure profiles and, consequently, the poloidal conductive and convective heat transport in the SOL. As a result, up-down asymmetries of 52:48 and 58:42 biased towards the outer lower and upper inner divertors, respectively, were observed to arise in the unmitigated power entering the divertor regions, breaking the up-down symmetry seen in simulations without the drift terms and contradicting with earlier experimental observations on the low-field side. Moreover, the upstream electron density was found to decrease noticeably in the core and separatrix regions following the activation of the drifts due to an increased share of the neutrals arriving from D_2 injections near the upper and lower X-points ionizing already in the private flux regions.

Keywords: fusion, STEP, divertor, drifts, SOLPS-ITER

(Some figures may appear in colour only in the online journal)

1. Introduction

Spherical Tokamak for Energy Production (STEP) [1, 2] is a prototype fusion power plant planned to be built in the UK by the 2040 s, aiming at production of net energy. In preparation for the significantly higher powers of power plant operation with respect to the present-day fusion experiments—with approximately 150 MW expected to cross the separatrix from the core plasma to the scrape-off layer (SOL) — the design of the divertor structure and operation scenarios is an area of specific focus to protect the integrity of the divertor targets under potentially destructive heat loads. In the current plan, adoption of double-null configuration and Ar impurity seeding are seen as the primary ways for provision of favorable divertor conditions.

* Author to whom any correspondence should be addressed.

The design of the divertor operations in STEP has been guided by predictive modeling with the SOLPS-ITER code package [3, 4], consisting of the fluid code B2.5 for solving the plasma conditions coupled with the Monte Carlo code EIRENE for simulating neutral particles. While providing guidelines for various aspects of the divertor design [5, 6], the earlier modeling work has so far omitted the contribution of cross-field drifts due to the additional numerical challenges they impose on the simulations, leaving thus certain transport-related physical phenomena unaddressed. Specifically, drifts have previously been associated with experimental observations of up-down asymmetric distribution of power between the divertors in connected double-null configurations of DIII-D [7], MAST [8–11] and Alcator C-Mod [12], which—due to the foreseen easier maintenance access to the upper divertors—is an area of special interest also for the STEP design. This contribution builds on the previously gathered knowledge of divertor modeling for STEP, adding indications of the effects of the cross-field drifts through their activation in the SOLPS-ITER simulations with focus on the changes observed in the heat transport into the divertor regions and the distribution of power in the plasma.

2. Simulation setup

Cross-field drifts were activated in a connected double-null configuration, illustrated in figure 1, with the magnetic field aligned to steer the ion $\nabla B \times B$ drift towards the upper divertors. The rectangular B2.5 simulation grid comprised of 148 $\times$ 34 poloidal and radial cells, respectively, providing spatial resolutions of 70–80 cm and 0.2–1.0 mm in the respective directions near the separatrix at the midplanes and 10–13 cm and 1–3 mm correspondingly near the strike points. The triangular EIRENE grid intersected with the B2.5 grid and filled the space between its SOL and private flux region (PFR) boundaries and the wall surfaces with typical cell dimensions of $\sim$5 cm.

In the simulations, the plasma was fuelled with two D_2 injections of $5.0 \times 10^{22}\,\mathrm{s}^{-1}$ near both X-points with an additional D^+ ion flow of $3.2 \times 10^{22}\,\mathrm{s}^{-1}$ entering the simulation volume across the core boundary, mimicking the expected radial transport of ions from the core plasma. The latter was defined as a feedback boundary condition, setting the total ion flow across the core boundary with close to neoclassical poloidal variation in the flux density, which has previously been found to be compatible with running simulations with the drift terms active. Pumping of particles was implemented as specific surfaces in the outer divertors, as shown in figure 1, with the D_2 reflection coefficient set to 92%. An input power of 150 MW was imposed across the core boundary with equal division between the power carried by electrons and ions.

A simplistic radial transport scheme with anomalous radial diffusion coefficient of $D_\perp = 0.15\,\mathrm{m^2 s^{-1}}$ and electron and ion heat conduction coefficients of $\chi_{\perp,\mathrm{e}} = \chi_{\perp,\mathrm{i}} = 0.5\,\mathrm{m^2 s^{-1}}$ was applied spatially homogeneously without variation across the minor radius or ballooning dependence on the major radius. These coefficients had previously been selected to yield a heat

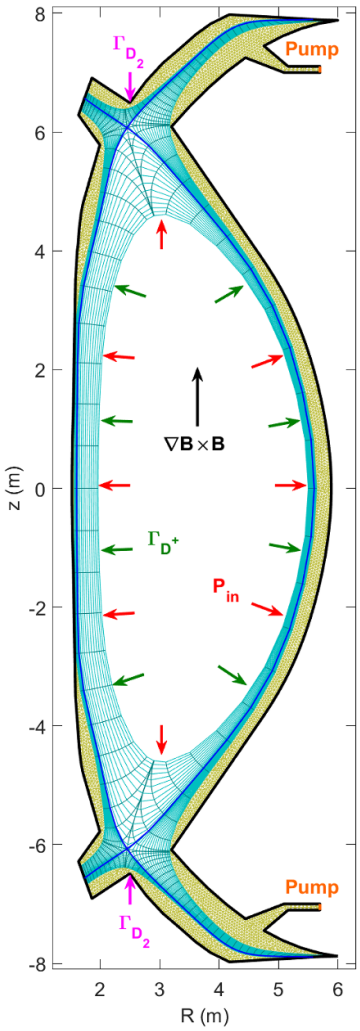

Figure 1. Plasma geometry in the SOLPS-ITER simulations, comprising of the B2.5 (cyan) and EIRENE (yellow) grids with the separatrix marked in blue. Note that the part of the EIRENE grid overlapping with the B2.5 grid is not plotted for clarity. The colored arrows illustrate the positions of the D_2 injections (magenta), as well as the input power (red) and the D^+ flux (green) across the core boundary. The pumping surfaces are marked with orange.

flux fall-off length of $\lambda_q \approx 2.0$ mm, which, however, was not considered as a fixed constraint in this work. It is acknowledged that spatially constant radial transport parameters—omitting, e.g., the typically applied decrease in $D_\perp$ around the separatrix—are rarely suited for interpreting experimental plasmas, but with no reference provided by experimental data yet available for STEP, such approach was found sufficient for the initial drift studies reported in this work. Expanding the investigations with varied and more sophisticated radial transport assumptions is planned for future work. Flux limiters were active on poloidal heat transport associated with electrons, ions and viscosity with coefficients of 0.3, 1.0 and 0.5, respectively.

To simplify the process of the initial activation of the drift terms in high-power STEP plasmas, the Ar impurities were not tracked, but the simulations were run with pure D plasmas with the neutral particles treated kinetically by EIRENE. To mimic

the radiative losses resulting from the Ar seeding, an additional electron energy loss term $f_{\mathrm{Ar}} n_{\mathrm{e}}^2 L_{\mathrm{Ar}}(T_{\mathrm{e}})$ was included in the SOL and divertor regions, assuming a fixed Ar fraction of $f_{\mathrm{Ar}} = 0.5\%$. An ADAS [13] collisional-radiative model was used to calculate the radiative loss function, L_{Ar}, using ADAS 89 data and a non-coronal parameter of $n_{\mathrm{e}}\tau = 0.5 \times 10^{20}\,\mathrm{m}^{-3}\mathrm{ms}$ (see figure 3 of [14]). This alleviated the numerical challenges involved in activating the drifts and enabled indicative predictions of their effects, while the process of switching the drift terms on in simulations with fully tracked Ar impurities is ongoing. With the imposed fixed Ar fraction, both inner divertor targets were initially detached with target temperatures below 1.0 eV, while the outer divertors were in high-recycling conditions at $T_{\mathrm{e}} \leqslant 7.0$ eV. In addition to the simplified treatment of the Ar seeding, the speedup scheme presented in [15], involving increased anomalous electric conductivity, was applied to improve the numerical stability of the runs and to allow maintaining the time step of the simulations at a reasonable level of $\tau = 1.0 \times 10^{-7}$ s while the drift contributions were gradually ramped up.

Apart from the drift terms, the input parameters were kept the same between the simulations. While the additional drift-driven radial transport can be expected to yield deviations, e.g., already in the upstream density and temperature profiles—which in interpretative modeling with experimental reference data or predictive modeling with pre-defined constraints for, e.g., λ_{q} would typically be compensated by adjusting the anomalous transport coefficients and boundary conditions—the approach of fixed input parameters was chosen to limit the observed effects to those originating from the drifts alone. This allows more conclusive assessment of the robustness of the assumptions behind the drift-free predictions in different parts of the plasma against the addition of the drift terms in the simulations.

3. Effect of drifts on SOL density and temperature

3.1. Midplane region

Before the activation of the drift terms, the applied fuelling rate, input power, boundary conditions and radial transport coefficients resulted in separatrix electron density and temperature of $n_{\mathrm{e,sep,omp}} = 2.8 \times 10^{19}\,\mathrm{m}^{-3}$ and $T_{\mathrm{e,sep,omp}} = 280$ eV, respectively, at the outer midplane as shown in figures 2(*a*) and (*b*) With the drifts switched on—and allowing n_{e} to evolve freely at the core boundary with only the ion flow across the boundary fixed—the upstream n_{e} was observed to decrease by 10%–25% in the core, separatrix and near SOL regions with a corresponding increase of 15%–25% in T_{e} in the same regions. Figures 2(*c*) and (*d*) show the decrease of n_{e} and increase of T_{e} to occur monotonically throughout the gradual activation of the drift terms.

Despite the decreased density near the separatrix, the additional drift-driven transport results in the net radial transport source of ions from the separatrix region into the SOL remaining approximately the same within 5%. The significance of the drift terms in the main chamber SOL decreases rapidly with the distance from the separatrix due to the T_{i} proportionality of the $\nabla B \times B$ drift velocity and the magnetic field configuration making the far-SOL flux surfaces increasingly vertical near the X-points, further reducing the radial contribution of the $\nabla B \times B$ drift in the regions where its impact on the near SOL is the strongest. Consequently, apart from the proximity of the separatrix, the upstream SOL conditions primarily deviate by less than 5% between the simulations with and without the drifts.

The observed decrease of the core density suggests decreased efficiency of fuelling of the core plasma with the D_2 injections due to the drifts, which is supported by up to 40% decrease in the ionization source in the core with the drifts on. The effect is attributed to the PFRs becoming more opaque to the injected neutrals with the ionization in the PFRs increasing by approximately 20% after the activation of the drifts. This implies that the fuelling scheme to achieve given upstream conditions in STEP may deviate notably from predictions provided by simulations without the drift contributions with, e.g., increased pellet fuelling of the core plasma required to compensate for the decreased penetration of the divertor D_2 injections.

With the drifts active, the total particle content in the core plasma was 15% lower than initially without drits, the difference corresponding to approximately 9% of the total particle content in the entire simulation domain in the drift-free simulations. This is almost directly reflected on the 8% decrease observed in the total particle content in the simulation domain observed following the activation of the drifts, suggesting that the net effect of the particles omitted from the core is mostly balanced by pumping, such that the divertor, PFR and SOL regions primarily experience re-distribution of the particles between the regions due to the drifts rather than additional notable changes in their combined particle content.

3.2. Divertor volumes

Re-distribution of particles due to the drifts is reflected on the densities averaged over the SOL and PFR volumes of the four divertor regions in figure 3, calculated by dividing the total numbers of particles in each divertor region with the volumes of the respective regions. Without drifts, the simulations show higher densities in the inner than the outer divertors with approximately a 64:36 distribution, whereas the respective upper and lower divertor densities are in balance. With the activation of drifts, the volume-averaged density is observed to increase in the inner upper and outer lower divertor regions and decrease in the inner lower and outer upper divertors. This narrows the in-out density asymmetry in the lower divertor to 58:42 and widens it to 71:29 in the upper divertor, giving thus also rise to up-down asymmetries between the volume-averaged divertor densities.

The evolution of the volume-averaged divertor densities is in agreement with the schematic expectation of the drift directions in the divertor regions. The increasing or decreasing behavior of the density is observed to follow the direction of the radial $E_\theta \times B$ drift from the inner lower to the outer lower divertor and the outer upper to the inner upper divertor, while the trend is amplified or attenuated by the poloidal $E_{\mathrm{r}} \times B$ and

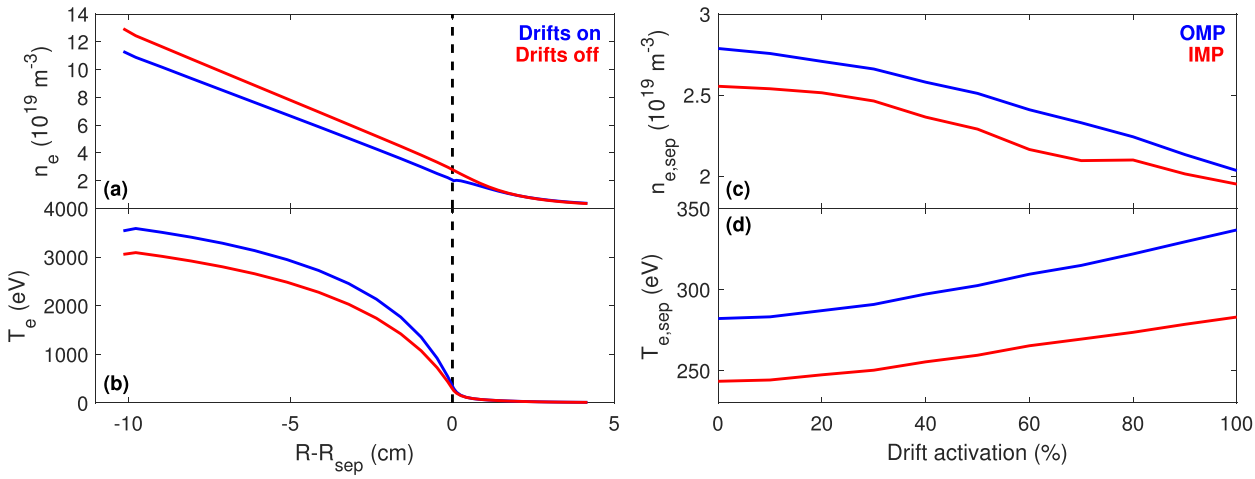

Figure 2. Radial profiles of the electron density (*a*) and temperature (*b*) at the outer midplane before (red) and after (blue) the activation of the drifts. The evolution of the separatrix electron density (*c*) and temperature (*d*) at the outer (OMP, blue) and inner (IMP, red) midplanes during the activation process of the drift terms.

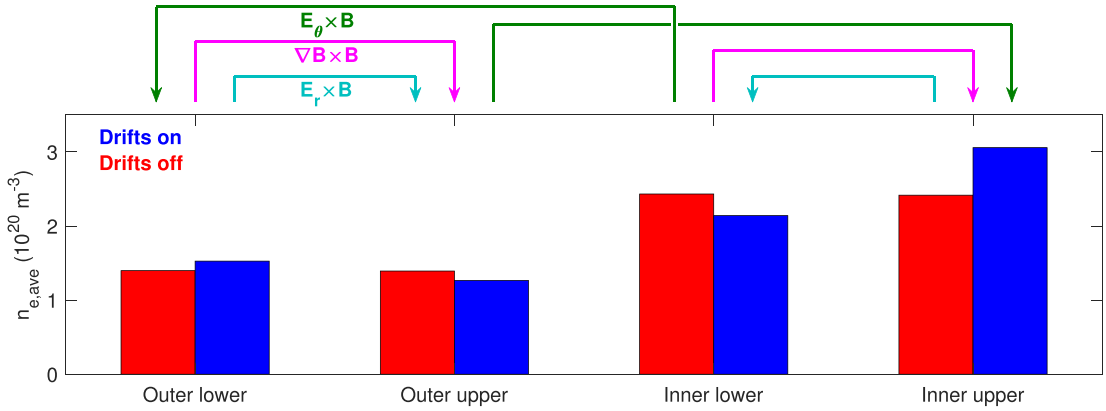

Figure 3. Volume-averaged electron densities in the different divertor regions before (red) and after (blue) the activation of the drift terms. The colored arrows represent the expected drift-driven ion transport between the divertor regions.

the vertical $\nabla B \times B$ drifts. Consequently, the relative changes in the volume-averaged densities are more significant on the high-field side (HFS), where both $E_\theta \times B$ and $\nabla B \times B$ drifts are feeding the upper divertor and draining the lower divertor, than on the low-field side (LFS), where the $E_\mathrm{r} \times B$ and $\nabla B \times B$ drifts act against the driving $E_\theta \times B$ drift, decreasing the net effect. The dominant role of the $E_\theta \times B$ drift in enhancing the divertor asymmetries is in agreement with previous analysis performed for, e.g., JET [16] and ASDEX Upgrade [17].

4. Effect of drifts on power flow symmetry at divertor entrances

4.1. Power asymmetries at divertor entrances

Precursors for the heat loads endured by the divertor targets are set by the unmitigated power flow into each divertor region prior to the volumetric losses occurring in the divertor plasma. As in the case of the volume-averaged densities, the powers entering the inner and outer divertors at the levels of the upper and lower X-points were equal between the respective upper and lower divertors in the simulations without drifts, as shown in figure 4, with the outer divertors receiving approximately 83% of the total power entering all four divertor volumes. With the drift terms activated, the powers entering the inner lower and the outer lower divertors are observed to decrease by 28% and increase by 8%, respectively, whereas the powers entering the upper divertors remain approximately unchanged within 1%–2% on both inner and outer side. Consequently, the in-out asymmetry in the power entering the lower divertor widens to 88:12, and up-down asymmetries arise on both sides with the upper inner and the outer lower divertors receiving more power according to 58:42 and 52:48 ratios, respectively. In absolute terms, the total power entering the four divertor volumes remained approximately the same with its share of the input power increasing only marginally from 93% to 94% following the activation of the drift terms. The small change can be attributed to the differences in the volumetric losses in the main chamber SOL due to the previously discussed changes in the upstream conditions.

Together with the density asymmetries discussed in section 3.2, the observations generally align with the key role

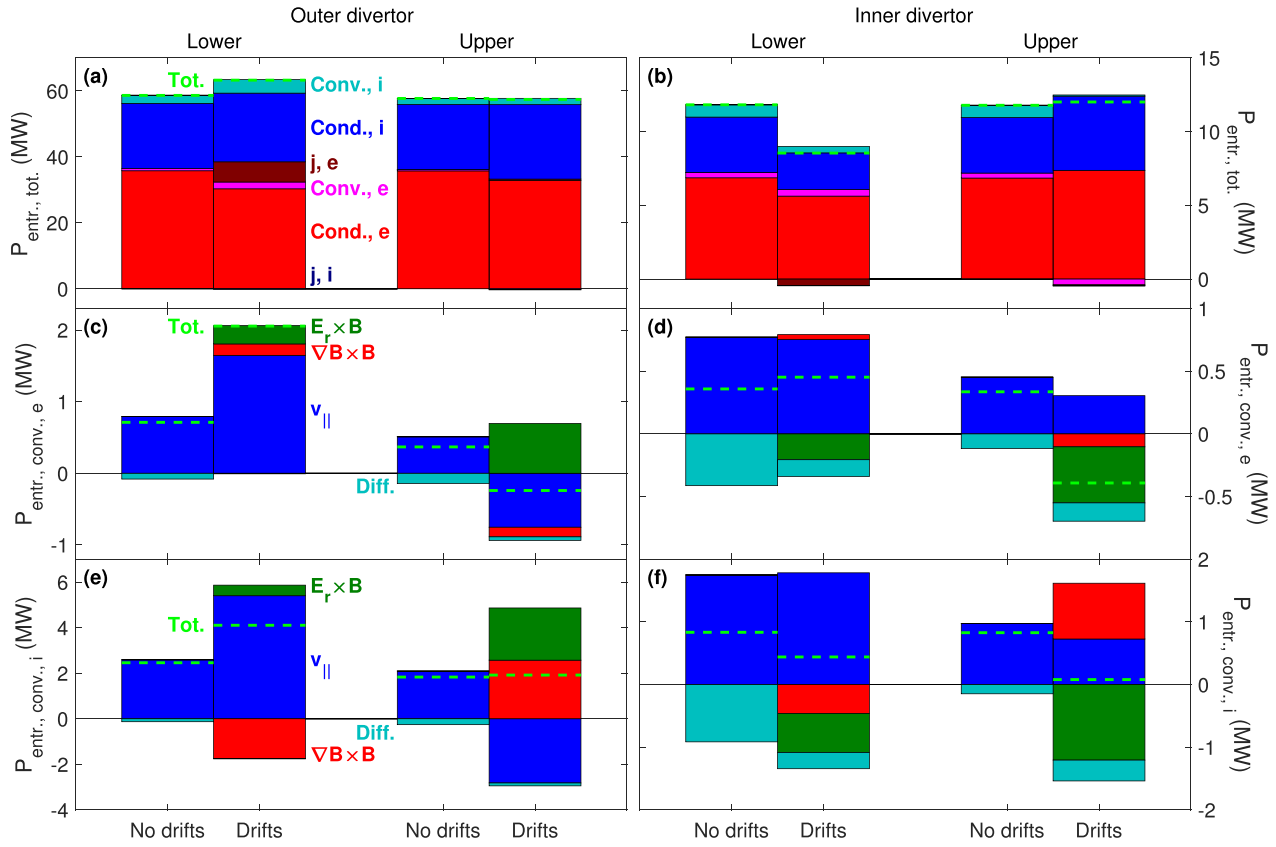

Figure 4. Unmitigated total powers entering the outer (*a*) and inner (*b*) divertor regions in the SOL at the level of the X-points before and after the activation of the drift terms, divided to the components attributed to electron (red) and ion (blue) heat conduction, convection via electron (magenta) and ion (cyan) transport and power carried by electrons (dark red) and ion (dark blue) due to the parallel current. Breakdown of the convective power flows to the outer (*c*), (*e*) and inner (*d*), (*f*) divertor regions carried by electrons (*c*), (*d*) and ions (*e*), (*f*) due to the parallel plasma flow (blue), diffusive particle transport (cyan) and the $E_r \times B$ (green) and $\nabla B \times B$ (red) drifts. The positive direction corresponds to power flow into the divertor volume, and the light green dashed lines indicate net power flows as sums of the distinguished components in each case. Note the varying *y* ranges in the different subplots.

that the drifts have widely been documented to have in predicting and interpreting experimentally observed appearance and enhancement of in-out and up-down asymmetries in a range of devices [16–21]. However, earlier experimental observations from DIII-D [7], MAST [8–11] and Alcator C-Mod [12] indicate expectations of the primary divertor—i.e., the lower divertor in the aforementioned studies and the upper divertor with the magnetic configuration of STEP—receiving approximately 60% of the power in the SOL in connected double-null configurations. While the simulations agree with this hypothesis for the inner divertors, on the outer side the bias of the up-down asymmetry towards the lower divertor is in contradiction with it.

It is noted that the aforementioned experimental analyses focused on plasmas with attached divertor conditions, as well as discuss the power reaching the divertor targets rather than the unmitigated power entering the divertor regions and consider the total up–down balance by summing the inner and outer divertors together. With similar approach, the simulations in this work with the drift terms active yield 51:49 and 61:39 up–down asymmetries, predicting more power reaching the lower divertor entrances and the target plates, respectively, with perfect 50:50 balance also at the target plates without drifts. Modeling work for assessing the power division in the event of re-attachment in STEP is ongoing, and the outcome of the simulations will be addressed elsewhere.

4.1.1. Outer lower divertor. As observed at all divertor entrances in figures 4(*a*) and (*b*), the power entering the outer lower divertor is dominated by the conductive components, particularly in the simulations without drifts in which the convective power flow accounts for only approximately 5% of the entrance power. The activation of drifts is observed to lead to an increase in the convective power flow carried by both ions and electrons, as well as appearance of a notable contribution of power carried by electrons associated with the parallel current, primarily driven by poloidal pressure and temperature gradients in the SOL plasma and accounting for approximately 16% of the power carried by electrons into the lower outer divertor. These components are sufficient to surpass the slight decrease in the power flow due to electron heat conductance and yield the previously discussed increase in the power entering the lower outer divertor.

Closer inspection of the convective power flow components for electrons and ions in figures 4(*c*) and (*e*) indicates their

increase to be primarily driven by an increase in the component associated with the parallel plasma flow. For ions, this increase is sufficiently strong to overcome the opposing effect of the $\nabla B \times B$ drift. It is noteworthy that while the expected direction of the poloidal $E_r \times B$ drift is away from the outer lower divertor, the total power carried by it is actually entering the divertor volume. This is due to the radial electric field, which is generally directed outwards in the SOL, changing its direction to inwards slightly outside the separatrix, consequently reversing the direction of the $E_r \times B$ drift in a narrow region in the proximity of the separatrix. Due to it being the hottest part of the SOL, this partial change of direction is sufficient to make the net power carried by the $E_r \times B$ drift enter the outer lower divertor rather than exit it.

4.1.2. Outer upper divertor. A small decrease in the power entering the outer upper divertor via electron heat conduction with the drifts active is compensated by a corresponding increase in the power conducted by ions, leaving the total power flow into the outer upper divertor approximately unchanged, as observed in figure 4(*a*). With the drifts on, the parallel plasma flow is directed towards the lower divertor already at the upper X-point, reversing the corresponding convective power flow components for electrons and ions in figures 4(*c*) and (*e*), respectively. However, the resulting change in the former is insignificant in comparison to the conductive heat transport, whereas the latter is balanced by the $E_r \times B$ and $\nabla B \times B$ drift contributions for zero net effect.

4.1.3. Inner lower divertor. The decrease in the power entering the inner lower divertor in figure 4(*b*) with the drifts active can be seen to result primarily from a decrease in the conductive components of both ion and electron heat transport with lesser effects from decreased convective power flow carried by ions and the parallel current driving power of electrons away from the divertor. Figures 4(*d*) and (*f*) show almost no change in the parallel flow into the inner lower divertor, while the contribution of the $E_r \times B$ and $\nabla B \times B$ drifts in the convective heat transport is largely compensated by decrease of power flow associated with diffusive particle transport for both electrons and ions. Consequently, the drifts do not have a noticeable net effect on the convective heat transport into the inner lower divertor, but the observed changes are driven by conduction.

4.1.4. Inner upper divertor. At the inner upper divertor entrance, figure 4(*b*) indicates increase in conductive heat transport into the divertor volume, especially in the case of ions. The increase is, however, balanced by convective heat transport, as the $E_r \times B$ drift reverts the direction of the convective power flow carried by the electrons and suppresses the convective transport carried by the ions in figures 4(*d*) and (*f*), respectively. In total, the power entering the inner upper divertor remains thus approximately unchanged after the activation of the drifts in figure 4(*b*).

4.2. Poloidal heat transport from main chamber to divertors

When the heat fluxes towards the divertors are inspected poloidally across the main chamber SOL, significantly stronger drift-related effects are observed around the midplane regions in figures 5(*a*) and (*b*) than at the divertor entrances discussed above. Here, the heat fluxes are calculated over the entire radial width of the SOL. Most notably, the stagnation points of the heat fluxes are found to move from the midplanes towards the upper divertors on both LFS and HFS, when the drifts are activated. This is predominantly attributed to the significant changes observed in the heat transport by ions, whereas the heat flux carried by the electrons shows relatively smaller differences between the simulations with the drifts off and on.

The most notable change in the heat flux carried by ions can be seen in the components associated with the parallel plasma flow in figures 5(*c*) and (*d*). Both on the LFS and HFS the parallel flow becomes significantly stronger with the drifts active and, instead of changing its direction at the midplane, is consistently directed towards the lower divertor across the main chamber SOL. On the LFS in figure 5(*c*), also the component due to ion heat conduction is found to deviate noticeably between the simulations with and without drifts and have its stagnation point move towards the upper divertor. On the HFS in figure 5(*d*), the conductive component shows a higher heat flux near the inner upper divertor entrance with the drifts active and a decrease near the inner lower divertor entrance, as observed also in the power entering the divertor regions in figure 4(*b*). The $E_r \times B$ drift plays a smaller role in the heat flux between the X-points, while components associated with the $\nabla B \times B$ drift and diffusive ion transport are insignificant with respect to the other components.

4.3. Radial heat and particle transport between core and SOL

The observed changes in the poloidal heat transport can largely be explained by changes in the radial heat and particle transport between the core and the SOL, primarily due to the $\nabla B \times B$ drift. Without the contribution of drifts, figures 6(*a*) and (*b*) show the heat flux between the core and the SOL to be directed consistently radially outwards between the X-points. As further seen in figures 6(*c*)–(*f*), the drift-free radial heat transport is predominantly conductive, with the convective component due to particle diffusion accounting for a notable contribution only for the ions at the LFS, and peaks at the midplanes with symmetrical decays towards the X-points.

With the drifts active, the $\nabla B \times B$ drift introduces a strong convective heat flux contribution which breaks the poloidal symmetry of the heat flux crossing the separatrix. Figures 6(*c*) and (*d*) show the ion $\nabla B \times B$ drift feeding power into the SOL near the upper X-point and draining it from the SOL near the lower X-point, being sufficiently dominant—particularly on the LFS—to re-shape the poloidal profile of the radial ion heat flux across the separatrix. For electrons, the direction of the $\nabla B \times B$-driven heat flux in figures 6(*e*) and (*f*) is opposite to and its magnitude lower than for the ions due to the $\nabla B \times B$

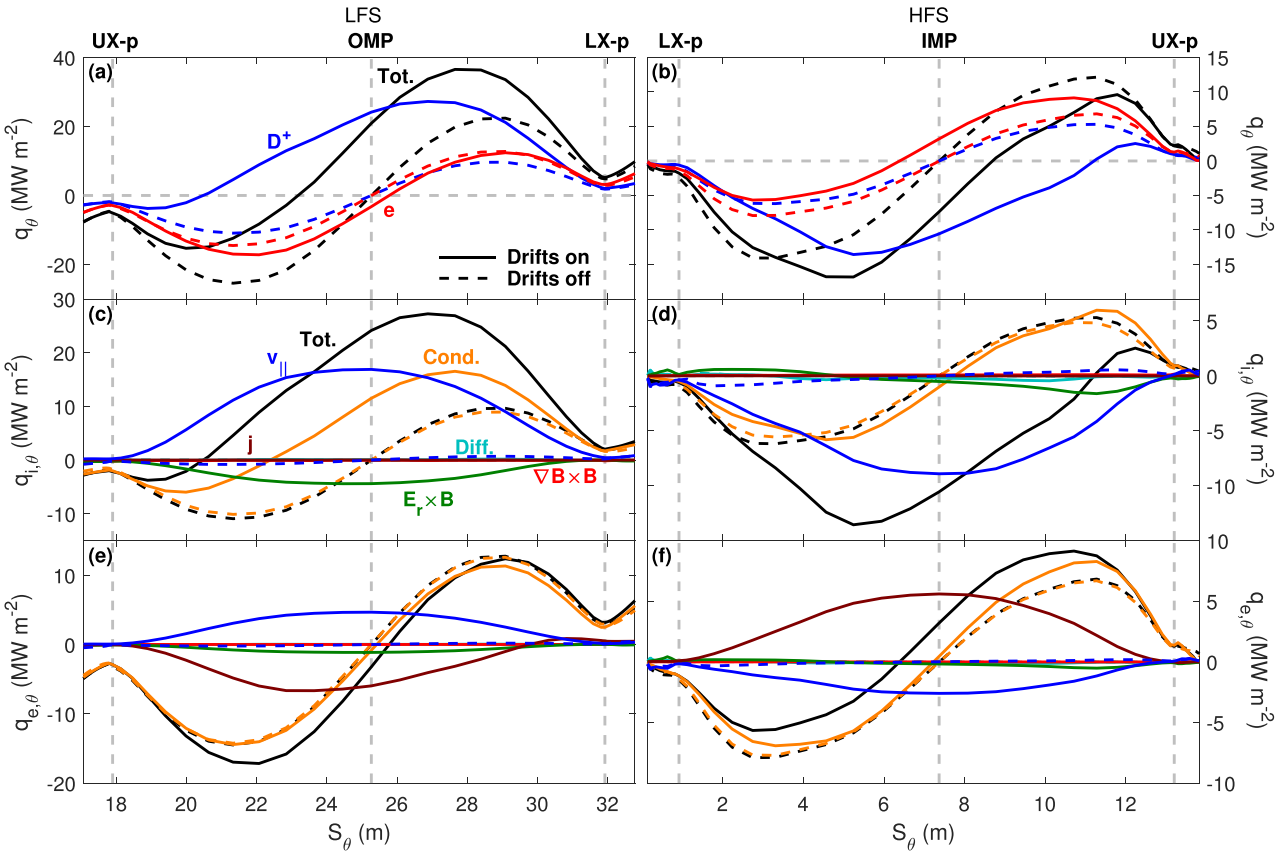

Figure 5. Poloidal heat fluxes across the LFS (*a*), (*c*), (*e*) and HFS (*b*), (*d*), (*f*) main chamber SOL before (dashed) and after (solid) the activation of the drift terms: total fluxes (black) divided to components carried by ions (blue) and electrons (red) (*a*), (*b*) and breakdowns of the ion (*c*), (*d*) and electron (*e*), (*f*) heat fluxes to components associated with conduction (orange), parallel plasma flow (blue), $\nabla B \times B$ drift (red), $E_\mathrm{r} \times B$ (green), particle diffusion (cyan) and parallel current (dark red). The coordinate S_θ measures the poloidal distance along the separatrix clockwise from the inner lower strike point, and the dashed grey lines mark the poloidal locations of the lower and upper X-points (L/UX-p) and the outer and inner midplanes (O/IMP). The positive direction of the heat flux is defined clockwise on the poloidal plane, i.e. towards the inner upper and outer lower divertors. Note the varying y ranges in the different subplots.

drift velocity being dependent on the charge and the temperature of the drifting species with $T_\mathrm{i,sep}$ exceeding $T_\mathrm{e,sep}$ by a factor of 2–3 in the main chamber. The strong effect on the ion heat flux is thus dominating the re-shaping of the total heat fluxes in figures 6(*a*) and (*b*), shifting the maximum of the radial heat transport from core to SOL from the midplanes towards the upper divertor and correspondingly decreasing—and at the LFS even reversing—it near the lower divertor.

The net effect of feeding and draining particles and heat near the upper and lower X-points, respectively, re-shapes the poloidal pressure profile in the SOL, shifting its maxima from the midplanes to the proximity of the upper X-point on both LFS and HFS. As a result, the arising pressure gradient drives an accelerated parallel plasma flow from the upper to the lower divertor on both sides, accounting for the observations of the corresponding heat flux components in figures 4 and 5. Moreover, the strong poloidal asymmetry in the ion heat flux between the core and the SOL in figures 6(*c*) and (*d*) is sufficient to shift the poloidal maxima of the ion temperature in the SOL from the midplane towards the upper X-point, explaining the corresponding shift of the stagnation points of the conductive poloidal ion heat fluxes in figures 5(*c*) and (*d*). The resulting changes in the poloidal profiles of T_e and T_i are also reflected on the conductive power flow components into the divertor regions in figures 4(*a*) and (*b*).

It is emphasized that the observations made above and the discussion on their impact on the poloidal heat transport are largely based on the transport of the main ions alone in absence of independently tracked impurities and are thus predicting an indicative basis on which the effect of the impurities remains yet to be added. Removing the assumption of the spatially homogeneous fixed fraction in the SOL and divertor plasma and thus de-coupling the Ar density and transport from the main ions can lead to significant changes in the distribution of impurities and the volumetric power losses they induce, consequently potentially affecting the poloidal temperature and pressure distributions and the heat fluxes driven by their gradients in the SOL. Moreover, the fixed-fraction model excludes the core region and limits the core radiation to bremsstrahlung only, omitting radiation by high ionization states of Ar potentially accumulating in the core plasma, which may further affect the total power crossing the separatrix into the SOL.

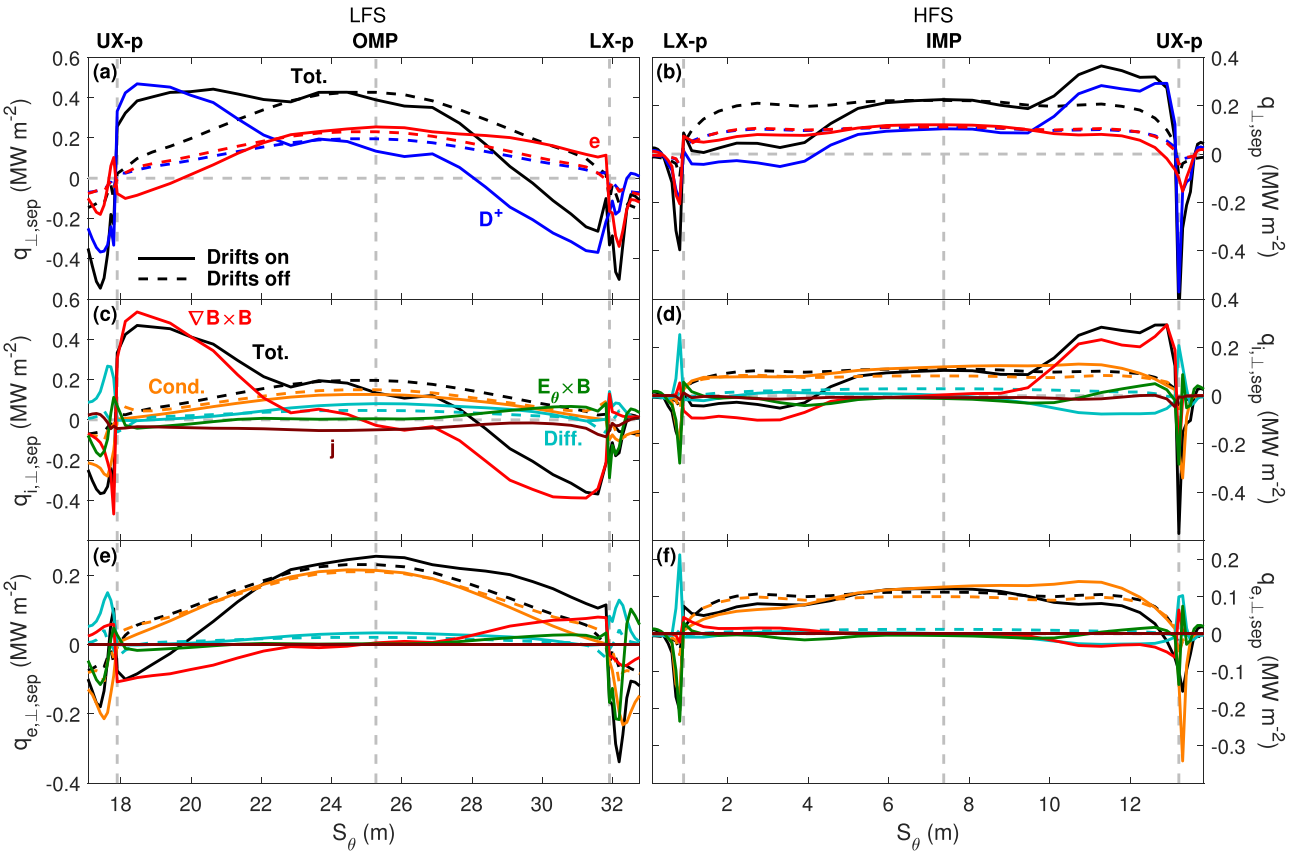

Figure 6. Radial heat fluxes across the separatrix into the LFS (*a*), (*c*), (*e*) and HFS (*b*), (*d*), (*f*) SOL before (dashed) and after (solid) the activation of the drift terms: total fluxes (black) divided to components carried by ions (blue) and electrons (red) (*a*), (*b*) and breakdowns of the ion (*c*), (*d*) and electron (*e*), (*f*) heat fluxes to components associated with conduction (orange), $\nabla B \times B$ drift (red), $E_\theta \times B$ (green), particle diffusion (cyan) and radial current (dark red). The coordinate S_θ measures the poloidal distance along the separatrix clockwise from the inner lower strike point, and the dashed grey lines mark the poloidal locations of the lower and upper X-points (L/UX-p) and the outer and inner midplanes (O/IMP). The positive direction of the heat flux is defined radially outwards from the core to the SOL. Note the varying y ranges in the different subplots.

5. Effect of drifts on divertor target conditions

At the outer lower divertor target, the radial profile of the electron density in figure 7(*a*) is found to be shifted towards the far SOL following the activation of the drift terms in agreement with the direction of the $E_\theta \times B$ drift similarly as previously observed, e.g., in experimental comparisons between forward and reversed field directions in DIII-D [22]. The shifting of the steep profile results in a strong decrease in the local n_e close to the outer lower strike point and in the PFR, leading to a notable increase in the peak target T_e approximately from 7 eV to 12 eV in figure 7(*b*). Consequently, while only a slight outwards shift is observed in the target ion flux in figure 7(*c*) similarly as for the target n_e, the maximum target heat flux at the outer lower strike point shows an increase by a factor of 2.0–2.5 in figure 7(*d*). The resulting peak heat load of $q_\mathrm{surf,osp} = 11.5\,\mathrm{MW\,m^{-2}}$ exceeds the safety limit of $10\,\mathrm{MW\,m^{-2}}$ set for the heat fluxes at the divertor surfaces, indicating potential need for protective measures—e.g., by increased Ar seeding—to preserve the integrity of the outer lower divertor components.

At the upper outer target, the radial profiles of n_e and Γ_{D^+} in figures 7(*e*) and (*g*) are shifted towards the PFR due to the $E_\theta \times B$ drift with a slight decrease of their peak value observed. Since the shift of the n_e profile does not result in similar decrease of density in the region of the T_e peak in figure 7(*f*) as at the outer lower target, similar strong increases of the maximum T_e and q_surf are not observed at the outer upper target in figures 7(*f*) and (*h*), but instead both are slightly decreased with the drifts activated.

Both lower and upper inner divertors were detached with $T_\mathrm{e} < 1.0$ eV prior to the activation of the drifts, as shown in figures 7(*j*) and (*n*), and no changes in the peak temperatures are seen following the activation of the drifts. However, strong decreases in the peak n_e, Γ_{D^+} and q_surf by factors of 2–3 are observed at both inner targets in figures 7(*i*) and (*k*)–(*p*), indicating an advanced state of detachment, where the region of the highest divertor density has shifted from the vicinity of the target upstream towards the X-point, decreasing n_e and Γ_{D^+} at the target. In the upper inner divertor, where the shift coincided with the strong overall increase in n_e in the divertor volume observed in figure 3, this resulted in increased

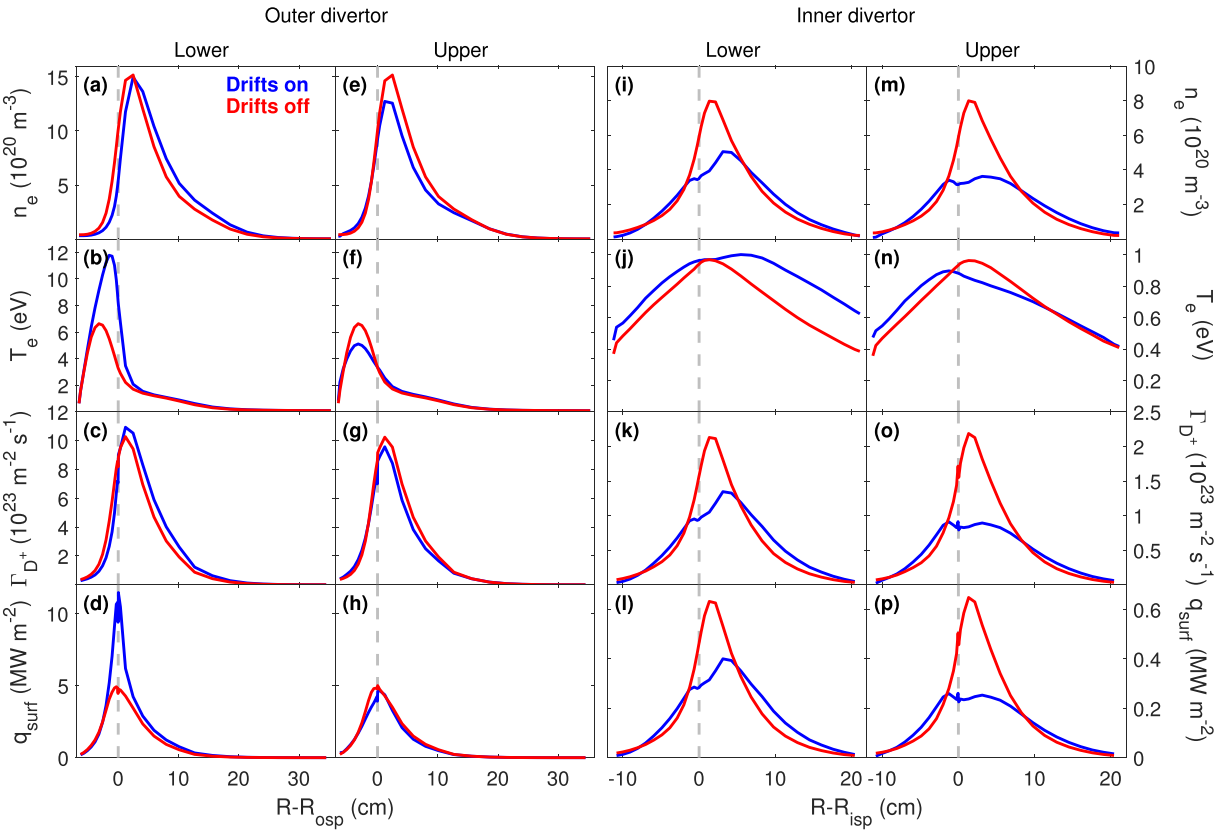

Figure 7. Radial profiles of the electron density (*a*), (*e*), (*i*), (*m*), electron temperature (*b*), (*f*), (*j*), (*n*) and poloidal ion (*c*), (*g*), (*k*), (*o*) and surface heat (*d*), (*h*), (*l*), (*p*) fluxes at the outer lower (*a*)–(*d*), outer upper (*e*)–(*h*), inner lower (*i*)–(*l*) and inner upper (*m*)–(*p*) divertor targets before (red) and after (blue) the activation of the drift terms. The dashed grey line marks the position of the strike point, and the $R - R_{\mathrm{o/isp}}$ coordinate measures the distance from the outer/inner strike point (O/ISP) along the target plate with positive values in the SOL and negative in the PFR.

volumetric power losses close to the X-point, resulting in a decrease in the power reaching the target, despite figure 4(*b*) showing practically no change in the power entering the divertor following the activation of the drift terms. In the lower inner divertor, similar increase in the volumetric losses is not observed, but the decrease in the target power flux reflects the decrease in the power entering the divertor volume observed in figure 4(*b*).

6. Conclusions

Activation of the cross-field drifts in predictive SOLPS-ITER simulations in connected double-null configuration of STEP was found to enhance the detachment of the inner divertors, while having an opposite effect at the outer lower divertor due to an increase in temperature and heat flux following an $E_\theta \times B$-induced radial shift of the divertor density. A significant effect of the $\nabla B \times B$ drift on the radial heat transport between the core and the SOL was found to contribute in the poloidal heat transport from the main chamber SOL into the divertor regions, giving rise to an up-down power asymmetry with more power entering the lower divertor on the LFS against the expectations set by earlier experimental observations in double-null operations, highlighting the importance of the indirect effects of the drifts via the re-shaping of the poloidal pressure and temperature distributions in the SOL. In addition, the activation of the drifts was observed to decrease the efficiency of the divertor D_2 injections for fuelling the core, leading to a decrease of the upstream density and a corresponding increase in the upstream temperature in the core and separatrix regions.

Currently still in lack of experimental data to validate against and modeling with drifts activated across a wider range of the simulation parameter space for STEP, the results presented in this work should be considered as first indications of the potential effects of the cross-field drifts to be considered in simulation work aiming at predicting divertor and SOL conditions in STEP. For instance, the observed strong initial role of radial particle and heat transport in the power flow to the divertors sets demand for further scan of the anomalous radial transport coefficients—including adoption of more experimentally relevant spatially varying transport assumptions and the ballooning model—as well as well-defined constraints for the upstream conditions during the activation of the drifts to enable more definite assessment of the drift effects on the divertor conditions without the observed strong impact on upstream n_e and T_e. Moreover, the simulations discussed in this work do not yet address the second-order effects due to the re-distribution of the Ar impurities and their radiation independently of the main D plasma. A wider range of divertor

conditions needs also to be investigated for improved assessment of the discrepancies in the up-down power asymmetries to the earlier experimental observations made in attached conditions. Work to adopt the drifts in SOLPS-ITER simulations with the impurity species fully tracked, as well as with attached divertor conditions, is ongoing.

Acknowledgments

This work has been part-funded by the EPSRC Energy Programme [Grant Number EP/W006839/1].

ORCID iDs

S.S. Henderson https://orcid.org/0000-0002-8886-1256
A. Järvinen https://orcid.org/0000-0002-4525-8158

References

[1] Wilson H. *et al* 2020 *Commecialising Fusion Energy* p 8-1–8-18
[2] Meyer H. 2023 The plasma scenarios for the spherical tokamak for energy production (STEP) and their technical implications *2023 IAEA Fusion Energy Conf.* (*London, UK*) [TH/P6-1]
[3] Wiesen S. *et al* 2015 *J. Nucl. Mater.* **463** 480–4
[4] Bonnin X. *et al* 2016 *Plasma Fusion Res.* **11** 1404102
[5] Osawa R.T. *et al* 2023 *Nucl. Fusion* **63** 076032
[6] Osawa R.T. *et al* 2024 Assessment of the impact of fuelling puff location on divertor impurity compression and enrichment in STEP *Nucl. Fusion* accepted
[7] Lasnier C.J. *et al* 1998 *Nucl. Fusion* **38** 1225
[8] Counsell G.F., Ahn J.-W., Akers R., Arends E., Buttery R., Field A.R., Gryaznevich M., Helander P., Kirk A., Meyer H., Valovic M. and Counsell G.F. 2002 *Plasma Phys. Control. Fusion* **44** B23–B37
[9] Kirk A. *et al* 2004 *Plasma Phys. Control. Fusion* **46** 551–72
[10] Meyer H. *et al* 2005 *Plasma Phys. Control. Fusion* **47** 843–67
[11] De Temmerman G. *et al* 2010 *Plasma Phys. Control. Fusion* **52** 095005
[12] Brunner D., Kuang A.Q., LaBombard B. and Terry J.L. 2018 *Nucl. Fusion* **58** 076010
[13] Summers H.P. 2004 The ADAS User Manual (version 2.6) (available at: http://www.adas.ac.uk)
[14] Kallenbach A. *et al* 2016 *Plasma Phys. Control. Fusion* **58** 045013
[15] Kaveeva E. *et al* 2018 *Nucl. Fusion* **58** 126018
[16] Chankin A.V. *et al* 2015 *Plasma Phys. Control. Fusion* **57** 095002
[17] Aho-Mantila L. *et al* 2017 *Plasma Phys. Control. Fusion* **59** 035003
[18] Rognlien T.D. *et al* 1999 *J. Nucl. Mater.* **266–269** 654–9
[19] Rognlien T.D. *et al* 2017 *Nucl. Mater. Energy* **12** 44–50
[20] Chen Y.P. *et al* 2011 *Phys. Plasmas* **18** 062506
[21] Aho-Mantila L. *et al* 2022 *Nucl. Fusion* **62** 056015
[22] Järvinen A. *et al* 2019 *Nucl. Mater. Energy* **19** 230–8